Ternary Organic Photodetectors Based on Pseudo-Binaries Nonfullerene-based Acceptors

Tianyi Zhang[1], Maximilian Moser[2], Alberto D. Scaccabarozzi[3], Helen Bristow[2], Polina Jacoutot[1], Andrew Wadsworth[2], Thomas D. Anthopoulos[3], Iain McCulloch[2,3], Nicola Gasparini[1]*

[1]Department of Chemistry and Centre for Processable Electronics, Imperial College London, W12 0BZ, UK

[2]Department of Chemistry, Chemistry Research Laboratory, University of Oxford, Oxford, OX1 3TA, UK

[3]King Abdullah University of Science and Technology (KAUST), KAUST Solar Center (KSC), Thuwal, 23955, Saudi Arabia

Corresponding author email: n.gasparini@imperial.ac.uk

Keywords: Organic photodetectors; nonfullerene acceptors; ternary blends; miscibility; scalable fabrication method.

Abstract

The addition of a third component to a donor:acceptor blend is a powerful tool to enhance the power conversion efficiency of organic solar cells. Featuring a similar operating mechanism, organic photodetectors are also expected to benefit from this approach. Here, we fabricated ternary organic photodetectors, based on a polymer donor and two nonfullerene acceptors, resulting in a low dark current of 0.42 nA cm^{-2} at -2 V and a broadband specific detectivity of 10^{12} Jones. We found that exciton recombination in the binary blend is reduced in ternary devices due to the formation of a pseudo-binary microstructure with mixed donor-acceptor phases. With this approach a wide range of intermediate open-circuit voltages is accessible, without sacrificing light-to-current conversion. This results in ternary OPD with improved R values in the NIR. Moreover, morphology analyses reveal that ternary OPD devices showed improved microstructure ordering and consequentially higher charge carrier mobilities compared to the reference devices.

Introduction

The organic photodetector (OPD), a technology based on organic photodiodes and therefore similar to organic photovoltaics (OPV), is an exciting new venture for organic semiconductor applications.[1–5] Through judicious design, the device can be tailored to multiple demanding applications for next-generation image sensing,[6,7] optical communication,[7] and medical implants.[8–10] Compared to conventional donor:acceptor OPDs, a ternary organic photodetector (TOPD) is the result of the introduction of a third component into its active layer.[11–13] To maximize OPD device performance, initial efforts have been made to transfer the successful strategies in the fabrication of efficient ternary organic photovoltaic (TOPV) devices to photodetection enhancement.[14] By chemically engineering the active layer, TOPD can obviate the need for a demanding and high-cost tandem structure to achieve broadband detection.[15] Exploiting complementary absorption, whereby the third component absorbs at different wavelengths when compared to the binary system, the ternary strategy can greatly extend the spectral response to the near-infrared (NIR) region.[16–20] Besides panchromatic absorption, the addition of the third component can also boost the current detection range performance through photocurrent enhancement thereby incurring a higher responsivity (R), specific detectivity (D*), wider linear detection range (LDR), and shorter transient time.[21–23] Indeed, ternaries can give rise to an increased number of pathways and interfaces that facilitate exciton dissociation and thus elevated photocurrent generation. A higher short-circuit current density (J_{sc}) can also be obtained

by exploiting the photon absorption capability of the third component to help generate more excitons through energy transfer.[24] Meanwhile, the energetic levels of donor and acceptor binary blends could also benefit from the mixing of the third component to achieve enhanced charge transfer and reduced trap states at the interfaces.[25,26] Such improvements are imperative for mitigating recombination to effectively reduce the dark current.[27–30] In addition to the energetics of the active materials, the blend microstructure is also of paramount importance. The incommensurate gain in external quantum efficiency, specific detectivity, and dark current presented in past studies shed light on the morphological variation with the incorporation of the third component. Depending on its crystallinity and miscibility with other components, the weight ratio (D:A1:A2 or D1:D2:A) of the additional component can impact the original structural order and the charge transport profile.[24,31–33] For instance, a finer morphology may be beneficial for charge generation and transport, but an intimate mixture of the components can aggravate charge recombination.[25,34,35] Therefore, key factors related to specific performance parameters should be stressed and prioritized when selecting the ternary component candidate to fully implement its role in the blend as well as retain the level of satisfaction for other figure of merits (FOMs). To date, a limited amount of literature has reported the ternary strategy for nonfullerene (NFA) TOPD compared with its fullerene counterparts. For fullerene-based blends, the typical design strategy for the third component is to extend the absorption window of the donor:fullerene blend by incorporating NIR absorbing polymers or small molecules.[36–38] However, adding low bandgap materials limits the V_{OC} of the devices, with a detrimental effect on dark

current (J_d).[39] The recent advent of NFAs has led to a number of further opportunities in ternary devices, owing to the variety of tunable energy levels, absorption profiles and crystallity.[40] Benefiting from a variety of donor and NFA combinations with the know-how developed for OPV,[41–44] the ternary approach can be a natural step for simultaneously improving multiple FOMs of organic photodetectors.

In this work, we have successfully demonstrated the realization of broadband spectral response through a ternary blend consisting of the donor polymer PTQ10[45] and two NFAs, namely O-IDTBR[46] and O-FBR.[47] Through optimizing the blend composition, a reduced dark current level, an improved flat responsivity and specific detectivity are obtained. In particular, the poor light-to-current conversion in the PTQ10:O-IDTBR binary blend due to the negative HOMO-HOMO offset, is addressed with the addition of the third component which facilitates charge transfer from the NIR acceptor.[48] This results in TOPD with D* exceeding 10^{12} Jones in the 350-730 nm spectral region. Moreover, higher charge carrier mobility is observed in the ternary blend due to the increased structural order and improved crystallinity that enhances charge transport. Wide linear dynamic range and promising frequency response are also presented. Thus, judicious selection and incorporation of a third component into binary OPD blends to create a TOPD can be a powerful tool to propel the engineering of high performance OPD.

Results and discussion

The photoactive layer of the ternary OPD studied comprises the donor polymer PTQ10 and different O-FBR:O-IDTBR (A1:A2) ratios. The chemical structures of the materials used, and their respective energy levels are depicted in **Figure 1a** and **1b**, respectively. We have previously shown that OPD devices based on PTQ10:O-FBR and PTQ10:O-IDTBR delivered low J_d in the order of nA cm^{-2} at -2 V.[48] However, despite a high responsivity of 0.42 A W^{-1}, PTQ10:O-FBR delivered light-to-current conversion only in the visible spectral region, preventing its application for near-infrared applications. On the contrary, PTQ10:O-IDTBR binary blends showed spectral coverage up to 750 nm, however, the negligible HOMO-HOMO offset between the donor and acceptor materials prevented efficient exciton dissociation, resulting in R values of 0.05 A W^{-1}. To overcome this limitation, we adopted the ternary strategy by blending PTQ10:O-FBR:O-IDTBR in different D:A1:A2 ratios with the aim of extending the absorption window of PTQ10:O-FBR upon addition of O-IDTBR (**Figure 1c**) and, at the same time, suppress exciton recombination in PTQ10:O-IDTBR due to the deeper HOMO level of O-FBR compared to O-IDTBR, enabling a type-II offset to be achieved. Different operating modes have been proposed in ternary blends, depending on the energetics of the components, the phase structure and the location of the third component in the bulk microstructure.

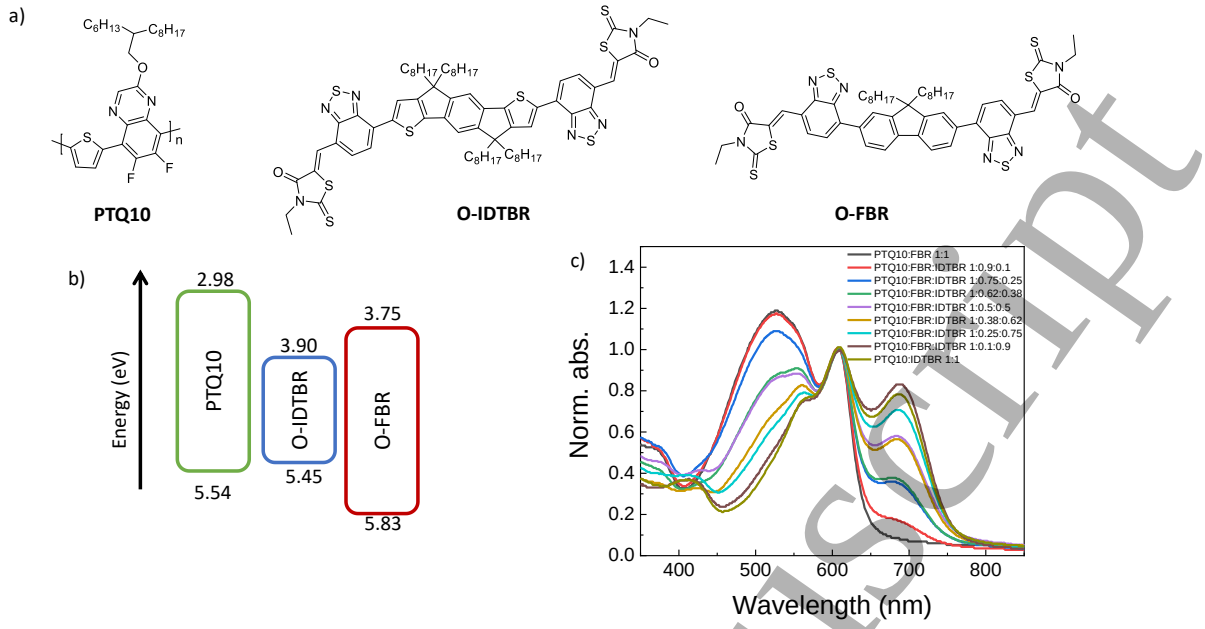

Figure 1. Chemical structures (a) and energy levels extracted from photoelectron spectroscopy in air measurements[48] (b) of PTQ10, O-IDTBR and O-FBR. (c) Absorption profiles of binary and ternary blends with different D:A1:A2 ratios.

To uncover the effect of the addition of the third component on OPD performance, we fabricated a range of ternary devices with different D:A1:A2 ratio. We adopted an inverted device structure consisting of indium tin oxide (ITO)/ZnO/Active layer/MoOx/Ag, with the photoactive layer blade coated in air. We first measured the current voltage (J-V) characteristics of the binary and ternary OPDs under one sun illumination (AM1.5G) and dark conditions (**Figure 2a** and **Figure S1**, in the supporting information). One of the photodetector's figures of merit is the J_d measured at a reverse bias of -2 V. Low J_d is necessary for sensing applications and maximizing the difference between dark and light current is therefore of utmost importance. **Figure 2b** shows the J_d values of binary and ternary blends at -2 V. In line with our previous

report, PTQ10:O-FBR and PTQ10:O-IDTBR delivered dark currents of 1.1 nA cm^{-2} and 1.8 nA cm^{-2}, respectively.[48] Interestingly, PTQ10:O-FBR:O-IDTBR (1:0.38:0.62) incurred the lowest J_d of 0.42 nA cm^{-2}, which can be related to the improved charge extraction or reduced charge recombination in the blend. In line with the concept of pseudo-binary blends,[14] we observed a range of intermediate V_{OC} around 1.18 V for PTQ10:O-FBR:O-IDTBR blends spanning from 1:0.85:0.15 to 1:0.38:0.62 (**Figure 2c**). In addition, as depicted by the responsivity curves in the reverse bias in **Figure 2d**, these ternary blends featured increased photocurrent compared to the binary PTQ10:O-IDTBR devices, likely due to improved exciton dissociation. As tabulated in **Table 1**, the R value at 710 nm of PTQ10:O-FBR:O-IDTBR (1:0.38:0.62) increased to 0.1 A W^{-1} compared to 0.06 A W^{-1} for PTQ10:O-IDTBR binary. Simultaneously, the addition of O-IDTBR into PTQ10:O-FBR allows a broader light-to-current conversion from 350 nm to 780 nm in the ternary blends, whereas the binary devices show R only in the 350-670 nm region.

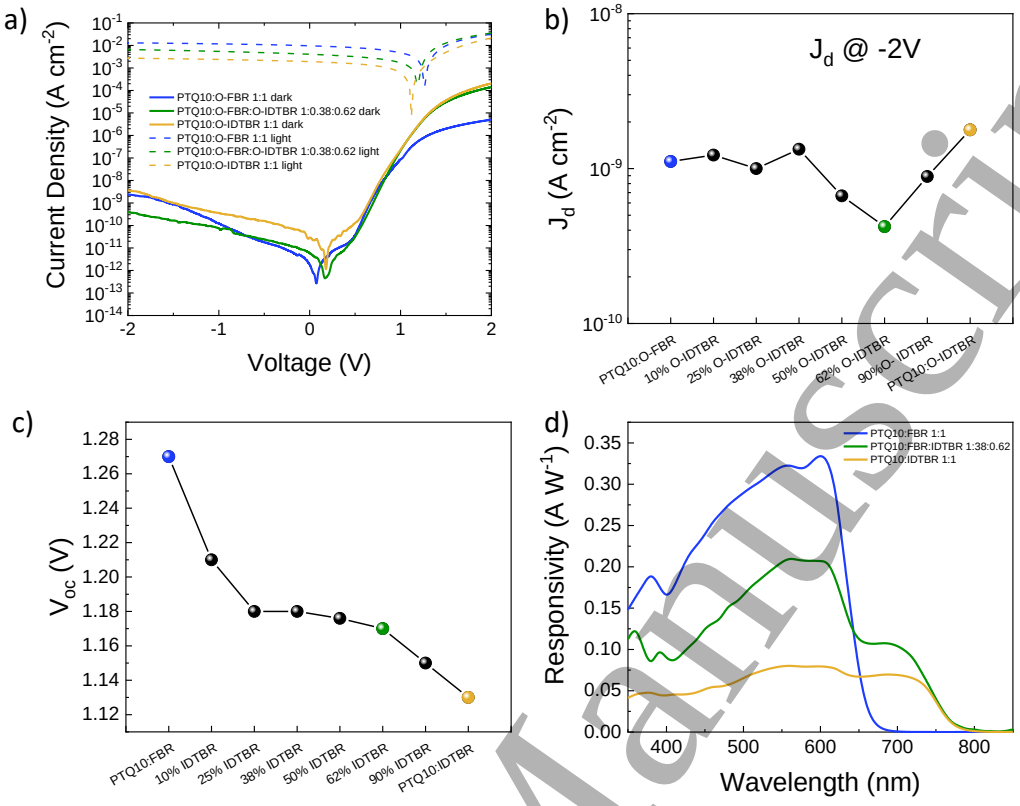

Figure 2. (a) Current-Voltage characteristics under dark and light conditions for binary and ternary blends. J_d at -2 V (b) and V_{OC} (c) for binary and ternary OPD devices. d) Responsivity values at -2 V for PTQ10:O-FBR, PTQ10:O-IDTBR and PTQ10:O-FBR:O-IDTBR 1:0.32:0.68.

Dark current values and responsivity are often used to calculate the specific detectivity (D*) of photodetectors, which provides insights into the signal stability and sensitivity of devices. However, J_d only reflects the shot noise of the devices, which results in overestimated D* values that do not take into account flicker and thermal noises. For this reason, we calculated the noise current (i_n), which can be calculated according to

equation 1, where q is the elementary charge, i_d is the dark current, k is the Boltzmann constant, T is the temperature, and R_{shunt} is the shunt resistance.[49]

$$(i_n)^2 = \left(2qi_d + \frac{4kT}{R_{shunt}}\right) \quad (1)$$

According to **Figure S2**, which shows the fast Fourier transform of the dark current, the noise floor has been reached at frequency as low as 0.1 Hz, suggesting that for frequencies above 0.1 Hz the flicker noise is negligible. D* can then be calculated according to equation 2, where A is the photodetector area and Δf is the measurement system bandwidth.

$$D^* = \frac{\sqrt{A\Delta f}R}{i_n} \quad (2)$$

Figure 3a shows the D* as a function of wavelength at -2 V for binary and ternary devices. Resulting from the extended light-to-current conversion, ternary devices delivered D* of 10^{12} Jones in the 350-730 nm range, while PTQ10:O-IDTBR shows D* of $2x10^{11}$ Jones across the same wavelength range. The results obtained for PTQ10:O-FBR:O-IDTBR are promising for applications that require detection across the UV-Vis-NIR spectral region, without the need of color filters, normally used for inorganic semiconductors.

Real world products, such as video imaging applications, require high contrast and fast response speed. These two properties are associated with the light dynamic range (LDR) and the cut-off frequency (**Figures S3-S5**). LDR is defined as the ratio between the photocurrent ($J_{ph}=J_l-J_d$, where J_d and J_l are the current densities under light and dark conditions, respectively) at high (j_{max}) and low (j_{min}) light intensities, according to $LDR=20\log(j_{max}/j_{min})$. **Figure 3b** shows the LDR plots for binary and ternary devices.

A linear trend of photocurrent vs light intensity is observed down to a light intensity of $1x10^{-3}$ mW cm^{-2}. We calculated LDR values at -2 V of 72 dB, 72 dB and 62 dB for PTQ10:O-FBR, PTQ10:O-FBR:O-IDTBR and PTQ10:O-IDTBR, respectively, which is in agreement with the OPD metrics reported above.

The cut-off frequency of photodetectors is defined as the photoresponse drop of $1/\sqrt{2}$ of the maximum photocurrent intensity, known as -3 dB limit and calculated according to equation 3, where i_{max} is the maximum photocurrent intensity and i_{freq} is the photocurrent intensity for a specific frequency of incident light.

$$Damping = 20log\left(\frac{i_{max}}{i_{freq}}\right) \quad (3)$$

It is generally accepted that for video applications a cut-off frequency of 10 kHz is sufficient.[6] As depicted in **Figure 3c**, both binary and ternary blends exceed this threshold value, in particular, we calculate cut-off frequencies of 90 kHz for PTQ10:O-IDTBR and in excess of 100 kHz for PTQ10:O-FBR and the ternary blend.

Finally, to better understand the superior response speeds of PTQ10:O-FBR:O-IDTBR 1:0.38:0.62 than PTQ10:O-IDTBR, we measured the effective drift mobility (□) of the OPD devices using the charge extraction at the short-circuit method. As depicted in **Figure 3d**, PTQ10:O-IDTBR delivered a lower effective mobility compared to PTQ10:O-FBR:O-IDTBR and PTQ10:O-FBR devices. Moreover, the ternary blend showed □ values less dependent on the charge density compared to the binary devices, which suggest more ordered transport in the PTQ10:O-FBR:O-IDTBR devices.

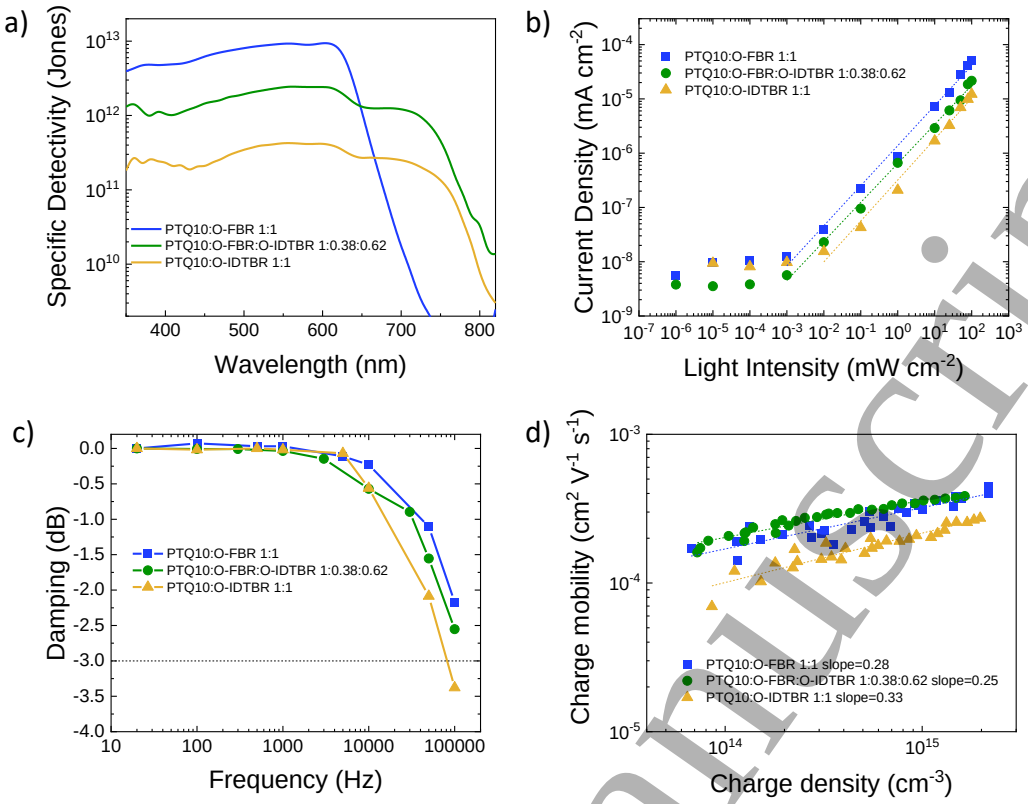

Figure 3. (a) Specific detectivity at -2 V for binary and ternary blends. LDR (b) and cut-off frequency (c) plots at -2 V for binary and ternary OPD devices. (d) Charge mobility vs charge density for PTQ10:O-FBR, PTQ10:O-IDTBR and PTQ10:O-FBR:O-IDTBR 1:0.32:0.68.

Table 1. Key performance parameters for binary and ternary based OPDs including dark current density (J_d), responsivity (R), linear dynamic range (LDR), and specific detectivity (D*), all reported at -2 V reverse bias.

	J_d / A cm^{-2}	**R / AW^{-1} (@ λ / nm)**	**LDR / dB**	**D* / Jones (@ λ / nm)**
PTQ10:O-FBR (1:1)	1.1×10^{-9}	0.33 (605)	72	9.2×10^{12} (605)
PTQ10:O-FBR:O-IDTBR (1:0.38:0.62)	4.2×10^{-10}	0.21 (605) 0.10 (710)	72	2.4×10^{12} (605) 1.2×10^{12} (710)
PTQ10:O-IDTBR (1:1)	1.8×10^{-9}	0.06 (710)	62	2.3×10^{11} (710)

To elucidate the operating mechanism of PTQ10:O-FBR:O-IDTBR, we first carried out differential scanning calorimetry (DSC) measurements. **Figure S6** depicts the first heating and cooling DSC profiles of the neat materials, binary, and ternary blends. Consistent with previous literature,[45] PTQ10's thermogram is featureless over the evaluated temperature range thus indicating the absence of any measurable phase transitions upon heating or cooling. This is not the case for 1:1 binary blends employing either O-FBR or O-IDTBR as the acceptor, both of which incur melting endotherms in their first heating cycle. The recorded temperatures (T_m) of these melting peaks are 203 °C for the PTQ10:O-FBR blend and 228 °C for the PTQ10:O-IDTBR blend, which

coincide with the melting endotherms of neat O-FBR and O-IDTBR respectively.[46,47] The presence of these peaks is indicative of structural order and pure acceptor domains in the binary blends. Note that the recorded peak magnitude is significantly larger for the PTQ10:O-IDTBR binary blend, thus suggesting a greater degree of crystallinity present within the acceptor phase in this blend. In addition to a melting endotherm in the first heating cycle, the PTQ10:O-IDTBR blend also exhibits an exotherm at a temperature (T_c) of 128 °C, which previously has been ascribed to the crystallization of O-IDTBR.[46] Compared to the binary blends, the ternary PTQ10:O-FBR:O-IDTBR blend featuring a low fraction (1:0.62:0.38) of O-IDTBR is virtually featureless, with only poorly visible acceptor-related melting endotherms present at 193 °C and 217 °C, thus suggesting a much lower degree of order in the acceptor phase compared to the binary blend. On the other hand, similar to the binary PTQ10:O-IDTBR blend, the ternary PTQ10:O-FBR:O-IDTBR blend containing a high fraction (1:0.38:0.62) of O-IDTBR also features a visible O-IDTBR related melting endotherm in its first heating cycle. Compared to the binary blend, this transition, however, occurs at a lower temperature (T_m = 224 °C), extends over a broader temperature range and is smaller in magnitude, suggesting a lower purity of O-IDTBR domains, likely caused by the presence of the additional acceptor component (O-FBR). The depression of the O-IDTBR related crystallization peak from 128 °C in the binary to 124 °C in this blend further confirms this hypothesis.

To study the effect of the third component on the blend microstructure, we performed grazing incidence wide-angle X-ray scattering (GIWAXS) measurements. According to

our previous report,[48] the 2D GIWAXS pattern of PTQ10:O-IDTBR films (**Figure 4a**) showed distinct diffractions associated with both donor (q = 2.85 nm^{-1}) and acceptor (q = 3.68 nm^{-1}) components. PTQ10:O-FBR (**Figure 4b**) shows a clear diffraction associated to the donor, while no clear feature can be associated to the acceptor, suggesting a low degree of crystallinity of O-FBR, in line with the DSC measurements. The crystal structure of IDTBR is retained in PTQ10:FBR:IDTBR 1:0.38:0.62 films that show a well-defined diffraction at q = 3.68 nm^{-1}, mainly oriented in-plane, exhibiting a 2D GIWAXS pattern similar to that of the PTQ10:IDTBR binary, which is however missing in PTQ10:FBR:IDTBR 1:0.5:0.5 (**Figure 4d**) blends. The difference between the two ternary blends is better displayed in the in-plane scattering profiles reported in **Figure 4e**. In fact, PTQ10:O-IDTBR and PTQ10:O-FBR:O-IDTBR 1:0.38:0.62 films depict a similar reflection at q = 3.68 nm^{-1}, with a lower intensity in the ternary system, possibly due to the decreased amount of O-IDTBR,[48] while this peak is absent in the PTQ10:O-FBR:O-IDTBR 1:0.5:0.5. This suggests that in PTQ10:O-FBR:O-IDTBR 1:0.38:0.62, O-IDTBR tends to phase separate and crystallize, whereas in PTQ10:O-FBR:O-IDTBR 1:0.5:0.5 the two NFAs are relatively amorphous in nature, likely a result of mixing that disrupts the ordered packing of the individual NFAs; this is in line with the DSC analyses. The superior performances of PTQ10:O-FBR:O-IDTBR 1:0.38:0.62 can be attributed to a pseudo-binary microstructure. In fact, the ternary blend simultaneously features the main characteristics of the binary blends, i.e. high D* related to PTQ10:O-FBR and low J_d resulting from the superior microstructural order of PTQ10:O-IDTBR.

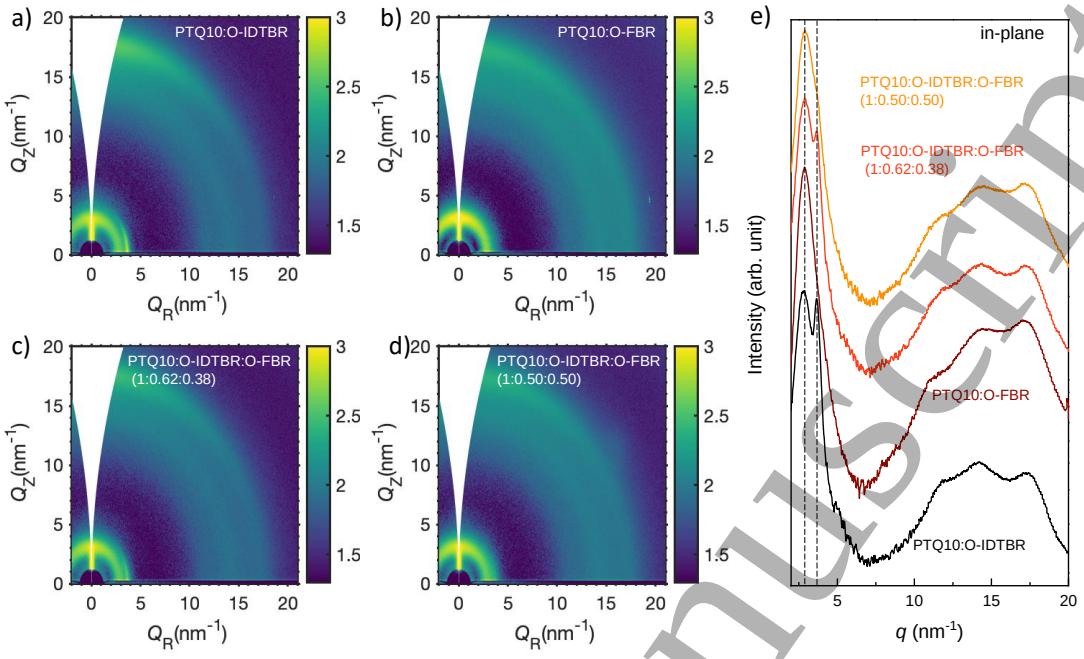

Figure 4. 2D GIWAXS patterns of (a) PTQ10:O-IDTBR, (b) PTQ10:O-FBR, (c) PTQ10:O-FBR:O-IDTBR 1:0.38:0.62 and (d) PTQ10:O-FBR:O-IDTBR 1:0.5:0.5. (e) In-plane scattering profiles integrated from the 2D-GIWAXS patterns.

In conclusion, we demonstrated an elegant design strategy to simultaneously extend the light-to-current conversion into the near-infrared and reduce the dark current in ternary organic photodetectors. We report PTQ10:O-FBR:O-IDTBR blends with D* in the excess of 10^{12} Jones in the 350-730 nm region and low dark current of 0.42 nA cm^{-2} at -2 V applied bias. We observed that introducing up to 38% by weight O-FBR in PTQ10:O-IDTBR mixtures suppresses exciton recombination in the blends due to the formation of a pseudo-binary configuration, resulting in improved R values in the NIR compared to PTQ10:O-IDTBR. Moreover, morphology analyses reveal that O-IDTBR

tends to crystallize rather than mix with O-FBR, which leads to a better microstructure ordering and consequentially high charge carrier mobility and reduced J_d. Our results show that the ternary approach is not only a useful tool for improving solar cells performances but can be also used to boost the photodetectors to real-world applications.

Acknowledgments

N.G. Acknowledges the Imperial College Research Fellowship Scheme. GIWAXS experiments were performed at BL11 NCD-SWEET beamline at ALBA Synchrotron (Spain) with the collaboration of Dr Eduardo Solano. The authors acknowledge financial support from KAUST, including Office of Sponsored Research (OSR) awards no. OSR-2018-CRG/CCF-3079, OSR-2019-CRG8-4086 and OSR-2018-CRG7-3749. We acknowledge funding from ERC Synergy Grant SC2 (610115), the European Union's Horizon 2020 research and innovation programme under grant agreement n° 952911, project BOOSTER, and grant agreement n° 862474, project RoLA-FLEX, as well as EPSRC Project EP/T026219/1.

References

1. Chow, P. C. Y. & Someya, T. Organic Photodetectors for Next-Generation Wearable Electronics. *Adv. Mater.* **32**, 1902045 (2020).
2. Strobel, N., Seiberlich, M., Eckstein, R., Lemmer, U. & Hernandez-Sosa, G. Organic photodiodes: printing, coating, benchmarks, and applications. *Flex. Print. Electron.* **4**, 043001 (2019).
3. Fuentes-Hernandez, C. *et al.* Large-area low-noise flexible organic photodiodes for detecting faint visible light. *Science (80-.).* **370**, 698–701 (2020).
4. Gasparini, N. *et al.* Visible and Near-Infrared Imaging with Nonfullerene-Based Photodetectors. *Adv. Mater. Technol.* **3**, 1800104 (2018).
5. Gasparini, N. *et al.* Adjusting the energy of interfacial states in organic photovoltaics for maximum efficiency. *Nat. Commun.* **12**, 1772 (2021).
6. Jansen-van Vuuren, R. D., Armin, A., Pandey, A. K., Burn, P. L. & Meredith, P. Organic Photodiodes: The Future of Full Color Detection and Image Sensing. *Adv. Mater.* **28**, 4766–4802 (2016).
7. Nath, D., Dey, P., Deb, D., Rakshit, J. K. & Roy, J. N. Fabrication and characterization of organic semiconductor based photodetector for optical communication. *CSI Trans. ICT* **5**, 149–160 (2017).
8. Rezaei-Mazinani, S. *et al.* Monitoring Intrinsic Optical Signals in Brain Tissue with Organic Photodetectors. *Adv. Mater. Technol.* **3**, 1700333 (2018).
9. Maya-Vetencourt, J. F. *et al.* A fully organic retinal prosthesis restores vision in a rat model of degenerative blindness. *Nat. Mater.* **16**, 681–689 (2017).

10. Maya-Vetencourt, J. F. *et al.* Subretinally injected semiconducting polymer nanoparticles rescue vision in a rat model of retinal dystrophy. *Nat. Nanotechnol.* **15**, 698–708 (2020).

11. Xu, W.-L. *et al.* Förster Resonance Energy Transfer and Energy Cascade in Broadband Photodetectors with Ternary Polymer Bulk Heterojunction. *J. Phys. Chem. C* **119**, 21913–21920 (2015).

12. Li, W. *et al.* Visible to Near-Infrared Photodetection Based on Ternary Organic Heterojunctions. *Adv. Funct. Mater.* **29**, 1808948 (2019).

13. Wadsworth, A., Hamid, Z., Kosco, J., Gasparini, N. & McCulloch, I. The Bulk Heterojunction in Organic Photovoltaic, Photodetector, and Photocatalytic Applications. *Adv. Mater.* **32**, 2001763 (2020).

14. Gasparini, N., Salleo, A., McCulloch, I. & Baran, D. The role of the third component in ternary organic solar cells. *Nat. Rev. Mater.* **4**, 229–242 (2019).

15. Baran, D. *et al.* Reducing the efficiency–stability–cost gap of organic photovoltaics with highly efficient and stable small molecule acceptor ternary solar cells. *Nat. Mater.* **16**, 363–369 (2017).

16. Yin, P., Yin, Z., Ma, Y. & Zheng, Q. Improving the charge transport of the ternary blend active layer for efficient semitransparent organic solar cells. *Energy Environ. Sci.* **13**, 5177–5185 (2020).

17. Zhan, L. *et al.* Over 17% efficiency ternary organic solar cells enabled by two non-fullerene acceptors working in an alloy-like model. *Energy Environ. Sci.* **13**, 635–645 (2020).

18. Yu, R. *et al.* Improved Charge Transport and Reduced Nonradiative Energy Loss Enable Over 16% Efficiency in Ternary Polymer Solar Cells. *Adv. Mater.* **31**, 1902302 (2019).

19. Nam, M. *et al.* Long-term efficient organic photovoltaics based on quaternary bulk heterojunctions. *Nat. Commun.* **8**, 14068 (2017).

20. Gasparini, N. *et al.* High-performance ternary organic solar cells with thick active layer exceeding 11% efficiency. *Energy Environ. Sci.* **10**, 885–892 (2017).

21. Wang, Y., An, T. & Xue, J. Realizing high detectivity organic photodetectors in visible wavelength by doping highly ordered polymer PCPDTBT. *Org. Electron.* **82**, 105700 (2020).

22. Fang, Y., Armin, A., Meredith, P. & Huang, J. Accurate characterization of next-generation thin-film photodetectors. *Nat. Photonics* **13**, 1–4 (2019).

23. Wu, Z. *et al.* Noise and detectivity limits in organic shortwave infrared photodiodes with low disorder. *npj Flex. Electron.* **4**, 6 (2020).

24. Gasparini, N. *et al.* Favorable Mixing Thermodynamics in Ternary Polymer Blends for Realizing High Efficiency Plastic Solar Cells. *Adv. Energy Mater.* **9**, 1803394 (2019).

25. Gasparini, N. *et al.* Designing ternary blend bulk heterojunction solar cells with reduced carrier recombination and a fill factor of 77%. *Nat. Energy* **1**, 16118 (2016).

26. Gasparini, N. *et al.* Exploiting Ternary Blends for Improved Photostability in High-Efficiency Organic Solar Cells. *ACS Energy Lett.* **5**, 1371–1379 (2020).

27. Simone, G. *et al.* On the Origin of Dark Current in Organic Photodiodes. *Adv. Opt. Mater.* **8**, 1901568 (2020).

28. Simone, G., Dyson, M. J., Meskers, S. C. J., Janssen, R. A. J. & Gelinck, G. H. Organic Photodetectors and their Application in Large Area and Flexible Image Sensors: The Role of Dark Current. *Adv. Funct. Mater.* **30**, 1904205 (2020).

29. Gielen, S. *et al.* Intrinsic Detectivity Limits of Organic Near-Infrared Photodetectors. *Adv. Mater.* **32**, 2003818 (2020).

30. Kublitski, J. *et al.* Reverse dark current in organic photodetectors and the major role of traps as source of noise. *Nat. Commun.* **12**, 551 (2021).

31. Naveed, H. B. & Ma, W. Miscibility-Driven Optimization of Nanostructures in Ternary Organic Solar Cells Using Non-fullerene Acceptors. *Joule* **2**, 621–641 (2018).

32. Jiang, K. *et al.* Multiple Cases of Efficient Nonfullerene Ternary Organic Solar Cells Enabled by an Effective Morphology Control Method. *Adv. Energy Mater.* **8**, 1701370 (2018).

33. Zhu, Y. *et al.* Rational Strategy to Stabilize an Unstable High-Efficiency Binary Nonfullerene Organic Solar Cells with a Third Component. *Adv. Energy Mater.* **9**, 1900376 (2019).

34. Zhou, Z. *et al.* High-efficiency small-molecule ternary solar cells with a hierarchical morphology enabled by synergizing fullerene and non-fullerene acceptors. *Nat. Energy* **3**, 952–959 (2018).

35. Lu, L., Xu, T., Chen, W., Landry, E. S. & Yu, L. Ternary blend polymer solar

cells with enhanced power conversion efficiency. *Nat. Photonics* **8**, 716–722 (2014).

36. Yang, Y. (Michael) *et al.* High-performance multiple-donor bulk heterojunction solar cells. *Nat. Photonics* **9**, 190–198 (2015).

37. Lu, L., Chen, W., Xu, T. & Yu, L. High-performance ternary blend polymer solar cells involving both energy transfer and hole relay processes. *Nat. Commun.* **6**, 7327 (2015).

38. Zhang, J. *et al.* Conjugated polymer-small molecule alloy leads to high efficient ternary organic solar cells. *J. Am. Chem. Soc.* **137**, 8176–8183 (2015).

39. Gasparini, N. *et al.* An Alternative Strategy to Adjust the Recombination Mechanism of Organic Photovoltaics by Implementing Ternary Compounds. *Adv. Energy Mater.* **5**, 1501527 (2015).

40. Wadsworth, A. *et al.* Critical review of the molecular design progress in non-fullerene electron acceptors towards commercially viable organic solar cells. *Chem. Soc. Rev.* **48**, 1596–1625 (2019).

41. Gasparini, N. *et al.* Polymer:Nonfullerene Bulk Heterojunction Solar Cells with Exceptionally Low Recombination Rates. *Adv. Energy Mater.* **7**, 1701561 (2017).

42. Gasparini, N. *et al.* The Physics of Small Molecule Acceptors for Efficient and Stable Bulk Heterojunction Solar Cells. *Adv. Energy Mater.* **8**, 1703298 (2018).

43. Wang, X. *et al.* Tuning the intermolecular interaction of A2-A1-D-A1-A2 type non-fullerene acceptors by substituent engineering for organic solar cells with ultrahigh V OC of ~1.2 V. *Sci. China Chem.* **63**, 1666–1674 (2020).

44. Tang, A. *et al.* Benzotriazole-Based Acceptor and Donors, Coupled with Chlorination, Achieve a High V OC of 1.24 V and an Efficiency of 10.5% in Fullerene-Free Organic Solar Cells. *Chem. Mater.* **31**, 3941–3947 (2019).

45. Sun, C. *et al.* A low cost and high performance polymer donor material for polymer solar cells. *Nat. Commun.* **9**, 1–10 (2018).

46. Holliday, S. *et al.* High-efficiency and air-stable P3HT-based polymer solar cells with a new non-fullerene acceptor. *Nat. Commun.* **7**, 11585 (2016).

47. Holliday, S. *et al.* A Rhodanine Flanked Nonfullerene Acceptor for Solution-Processed Organic Photovoltaics. *J. Am. Chem. Soc.* **137**, 898–904 (2015).

48. Bristow, H. *et al.* Nonfullerene-Based Organic Photodetectors for Ultrahigh Sensitivity Visible Light Detection. *ACS Appl. Mater. Interfaces* **12**, 48836–48844 (2020).

49. Strobel, N. *et al.* Color-Selective Printed Organic Photodiodes for Filterless Multichannel Visible Light Communication. *Adv. Mater.* **32**, 1908258 (2020).